



Three-dimensionally ordered macro-microporous metal organic frameworks with strong sulfur immobilization and catalyzation for high-performance lithium-sulfur batteries

Guoliang Cui^{a,b,1}, Gaoran Li^{c,1}, Dan Luo^c, Yongguang Zhang^{a,b,**}, Yan Zhao^{a,b}, Daorui Wang^a, Jiayi Wang^a, Zhen Zhang^c, Xin Wang^{a,***}, Zhongwei Chen^{c,*}

^a School of Information and Optoelectronic Science and Engineering, South China Academy of Advanced Optoelectronics, International Academy of Optoelectronics at Zhaoqing, South China Normal University, Guangzhou 510006, China

^b School of Materials Science and Engineering, Hebei University of Technology, Tianjin, 300130, China

^c Department of Chemical Engineering, University of Waterloo, Waterloo, ON, N2L 3G1, Canada

ARTICLE INFO

Keywords:

Lithium-sulfur batteries
Three-dimensionally ordered macro-microporosity
Metal organic framework
Adsorption
Catalyzation

ABSTRACT

Lithium-sulfur (Li-S) batteries have been recognized as one of the most promising technologies for next-generation energy storage. However, their practical implementation is greatly impeded by the sluggish sulfur kinetics and unsatisfactory cyclability. Herein, a novel three-dimensionally ordered macro-microporous metal organic frameworks (3DOM ZIF-8) is developed via self-templated coordination-replication method, which serves as an advanced sulfur reservoir for enhanced Li-S battery performance. The unique hierarchical architecture not only facilitates the electrolyte infiltration and ion/mass transportation, but also increases the surface area for abundant exposure of active interfaces. Moreover, the nanometric ZIF-8 subunits impose strong sulfur immobilization and catalyzation through their chemical interactions with polysulfides, thus rendering significantly inhibited shuttle effect and fast reaction kinetics. Benefiting from these synergistic features, sulfur electrodes based on 3DOM ZIF-8 exhibit excellent electrochemical performance, i.e., prolonged cycling stability with a low capacity decay of 0.028% per cycle over 500 cycles, as well as high areal capacity and decent cyclability under raised sulfur loading and limited electrolyte, demonstrating a great promise in developing practically viable Li-S batteries.

1. Introduction

Lithium-sulfur (Li-S) batteries have long been regarded as a promising next-generation energy storage system due to their high specific energy density (2500 Wh kg⁻¹), environmental benignity and low cost [1,2]. However, the widespread application of Li-S batteries is still obstructed by several major technical issues, which involve the insulating nature of sulfur, the dissolution and shuttling behaviors of the lithium polysulfide (LiPS) intermediates, and the large volume variation upon lithiation/delithiation process. As a result, the state-of-the-art Li-S batteries suffer from poor sulfur utilization, sluggish reaction kinetics,

and fast capacity fading [3–6].

Given this, porous materials have been extensively explored as sulfur reservoirs to suppress the LiPS shuttling effect [7,8]. The large surface area can benefit the sulfur homogenization, while the high porosity offers favorable physical sulfur confinement [9,10]. Among the various porous materials, metal-organic frameworks (MOF) have been recognized as a particularly promising candidate for high-efficiency sulfur immobilization. Benefiting from the ordered coordination between metal cations and organic ligands, MOF materials deliver unique architectural and surface chemical features for wide applications [11–15]. The metal sites and organic ligands of MOF materials are likely

* Corresponding author.

** Corresponding author. School of Information and Optoelectronic Science and Engineering, International Academy of Optoelectronics at Zhaoqing, South China Normal University, Guangzhou, 510006, China.

*** Corresponding author.

E-mail addresses: yongguangzhang@hebut.edu.cn (Y. Zhang), wangxin@scnu.edu.cn (X. Wang), zhwchen@uwaterloo.ca (Z. Chen).

¹ The authors contributed equally to this work.

to apply strong interactions with LiPS, which could help to strengthen the chemical sulfur confinement against the shuttling behaviors [16–18]. However, the majority of MOF bulks present large crystal size and predominant microporosity, which not only impedes the electrolyte infiltration and ion/mass transfers, but also limits the exposure of active sites for MOF-LiPS interactions. As a result, the MOF-based sulfur electrodes generally suffer from sluggish redox kinetics and poor cyclic stability [19]. Therefore, the rational design of MOF materials with highly dispersed active interfaces and enhanced macro/mesoporosity is of great necessity and significance for the improvement of MOF-based sulfur electrochemistry.

Recently, three-dimensionally ordered macro-microporous MOF materials (3DOM-MOF) have been emerging as promising candidates in energy storage and conversion applications owing to their overall good structural stability and unique architecture for expedite ion diffusion [20]. Meanwhile, the relatively open 3DOM construction benefits the efficient exposure of active sites, which facilitates the interfacial electrochemical processes [21]. In addition, the considerable macroporosity of the 3DOM framework could also favor the sulfur accommodation and buffer the volume expansion during lithiation/delithiation process [22, 23]. These favorable features endow 3DOM-MOF with intriguing potentials as sulfur reservoir, which also renders the development of well-tailored 3DOM-MOF structure highly desired.

Herein, we present a straightforward strategy to synthesize 3DOM ZIF-8 through a self-templated coordination-replication method, which serves as a multifunctional sulfur host material for improved Li-S batteries. The obtained 3DOM ZIF-8 well inherits the 3D ordered macroporous architecture, which is constructed by massive and uniformly dispersed ZIF-8 nano-subunits. Such ordered and synergistic integration of macroporosity and microporosity not only facilitates the electrolyte infiltration and charge/mass transportation, but also provides high surface area and abundant active sites for the chemical interactions between 3DOM ZIF-8 and LiPS. As a result, the as-developed 3DOM ZIF-8 imposes significantly enhanced sulfur immobilization and expedites sulfur conversion kinetics, contributing to a fast and stable sulfur electrochemistry. The sulfur electrodes based on 3DOM ZIF-8 exhibit excellent cycling stability over 500 cycles with a low capacity fading rate of 0.028% per cycle, and superb rate capability with a high capacity of 803 mAh g⁻¹ at 2 C. High areal capacity over 6 mAh cm⁻² and decent cyclability can be also achieved under raised sulfur loading and limited electrolyte. These results demonstrate a great promise of this strategy in promoting the practical application of Li-S batteries.

2. Experimental

2.1. Materials

All chemicals were used as received without further purification. Zinc nitrate hexahydrate (Zn(NO₃)₃·6H₂O, AR, 99%), anhydrous methanol (99.8%), and 2-Methylimidazole (98%) were purchased from Shanghai Aladdin Co., Ltd.

2.2. Fabrication of 3DOM ZnO

Poly(methyl methacrylate) (PMMA) nanospheres were firstly prepared as template according to our previous report [24]. Zn(NO₃)₃·6H₂O (3.56 g) was completely dissolved in anhydrous methanol (5 mL) under continuous stirring. Then, 2.25 g citric acid was added as chelating agent and stirred for 1 h. After that, PMMA (2.0 g) nanospheres were impregnated in the obtained solution and stirred for another 4 h. The resulting suspension was then vacuum filtrated to remove the excessive solution. After drying overnight at room temperature, the sample was thermally treated at 300 °C for 3 h in Ar atmosphere with a ramping rate of 1 °C min⁻¹. Subsequently, the sample was further heated at 300 °C for 3 h and 600 °C for 3 h successively under air atmosphere with a ramping rate of 1 °C min⁻¹. The yellow 3DOM ZnO

powders were collected after gradually cooling to room temperature.

2.3. Fabrication of 3DOM ZIF-8

3DOM ZnO (0.05 g) and 2-Methylimidazole (2.05 g) were added in anhydrous methanol (50 mL) and stirred at 60 °C for 8 h, upon which the yellow 3DOM ZnO gradually converted into white 3DOM ZIF-8.

2.4. Fabrication of ZIF-8

In a typical synthesis, 50 mL anhydrous methanol containing 1.5 g Zn(NO₃)₂·6H₂O and 25 mL anhydrous methanol containing 1.65 g 2-Methylimidazole was prepared separately and then mixed under stirring for 1 h at 25 °C. Then, the suspension was centrifugal washed with anhydrous methanol and dried at 60 °C overnight to obtain the ZIF-8 powder.

2.5. Fabrication of S/3DOM ZIF-8 and S/ZIF-8 composites

3DOM ZIF-8 (or ZIF-8) and sulfur were homogeneously mixed in weight ratio of 1:2. Then, the mixture was sealed and heated in tube furnace at 155 °C for 12 h to obtain the S/3DOM ZIF-8 (or S/ZIF-8) composite.

2.6. Material characterization

The morphology of the samples was investigated by scanning electron microscope (FESEM, JSM-7500, Japan) and transmission electron microscope (TEM, JEM-2100HR, JEOL). The thermogravimetric analysis of S/3DOM ZIF-8 and S/ZIF-8 composites was carried out on the TADTG Q600. The Brunauer-Emmett-Teller (BET, V-Sorb 2800P) was employed to analyze the surface areas and the pore-size distributions. The surface chemical states were studied by X-ray photoelectron spectroscopy (XPS, PHI 5000). The crystal structures were characterized by X-ray powder diffraction (XRD, Smart Lab, Rigaku). Fourier transform infrared spectroscopy was conducted on FT/IR-6000, Japan.

2.7. Electrochemical characterizations

The 2032-type coin cells were assembled in an Ar-filled glove box, comprising lithium metal anode (15.8 mm in diameter), Celgard 2400 separator and sulfur cathode. The cathode slurry was prepared by mixing S/3DOM ZIF-8 composites (80 wt%), Super-P (10 wt%) and poly(vinylidene fluoride) (PVDF, 10 wt%) in N-methyl-pyrrolidone (NMP) solvent. Then the slurry was casted on Al foil and dried at 60 °C overnight. The dried electrodes were cut into disks with a diameter of 12 mm for use. The typical sulfur loading is around 2.0 mg cm⁻². The electrolyte consists of 1.0 M lithiumbis(trifluoromethane sulfonyl) imide (LiTFSI) and 0.1 M LiNO₃ dissolved in a binary solvent of 1,3-dioxolane and 1,2-dimethoxymethane (DOL and DME, 1:1 by v/v). The amount of electrolyte was controlled at an electrolyte to sulfur ratio (E/S) of 15 mL g⁻¹ (33.9 μL per cell). For high-loading and limited-electrolyte characterizations, the electrolyte amount was reduced to the E/S ratio of 8.74 and 4.25 mL g⁻¹ under the sulfur loading of 3.6 and 7.4 mg cm⁻² (35.5 μL per cell), respectively. The cyclic voltammetry (CV) and electrochemical impedance spectroscopy (EIS) were performed on CHI660E, Shanghai. The CV curves were collected at a scanning rate of 0.1 mV s⁻¹, while the EIS spectra was obtained within the frequency range from 100 kHz to 0.01 mHz. Galvanostatic charge/discharge measurement was conducted by LAND CT2100A battery tester.

2.8. Symmetric cell test

The electrodes were prepared by casting the slurry containing 3DOM ZIF-8 (or ZIF-8) (80 wt%), Super P (10 wt%) and PVDF (10 wt%) in NMP solvent on carbon cloth. The identical electrodes were assembled in coin cells with the solution containing 0.1 M Li₂S₆ in DOL/DME (1:1 by v/v)

as electrolyte for the symmetric cell characterizations. The CV and EIS tests were performed on CHI760E workstation.

2.9. Li_2S nucleation test

The cell for Li_2S nucleation test was assembled by using the 3DOM ZIF-8 (or ZIF-8)-loaded carbon cloth as working electrode, lithium foil as counter electrode and Li_2S_8 (0.25 M)-contained electrolyte. The cells were first discharged galvanostatically at 0.112 mA to 2.06 V and then discharged potentiostatically at 2.05 V for Li_2S nucleation and growth. The potentiostatic discharge was terminated until the current decreased to 0.01 mA.

3. Results and discussion

Fig. 1 illustrates the synthetic route of 3DOM ZIF-8. The synthesis involves the construction of 3DOM ZnO framework by PMMA-templated infiltration and calcination processes, while the subsequent coordination by 2-methylimidazole ligand converts ZnO into ZIF-8 with well-inherited 3D ordered architecture (see details in Experimental). The scanning electron microscopy (SEM) image in Fig. S1a confirms the sophisticated nanospherical morphology of the as-prepared PMMA templates with good size uniformity. During the pyrolysis process, the soaked zinc nitrate precursor in the interspace tends to decompose and crystallize into ZnO, while the PMMA templates gradually decompose and evaporate leaving well-defined and ordered voids in the obtained architecture. During the conversion-replication process, the metal-ligand coordination generates the ZIF-8 nanocrystals along with the ZnO skeleton, constructing the ZIF-8-based framework with an inherent 3D ordered architecture, which well integrates the macroporosity of 3DOM and microporosity of ZIF8.

The morphology of 3DOM ZnO was unveiled by SEM and TEM

observations, which confirm its 3DOM structure with rich macroporosity (Fig. 2a and Fig. S1b). The HRTEM image in Fig. S1c shows the typical (101) and (100) lattice fringe of ZnO, indicating its good crystallized feature. The dark-field scanning TEM (STEM) and the corresponding elemental mapping images demonstrate the uniform Zn and O distributions in the product (Figs. S1d–f). These results indicate the successful formation of the interconnected 3DOM ZnO architecture without obvious structural collapse. The SEM and TEM images in Fig. 2b–c and Fig. S2 present the morphology of the obtained 3DOM ZIF-8, which shows the well-inherited 3DOM architecture from 3DOM ZnO, confirming the good structure integrity upon the coordination-replication process. Notably, the 3DOM ZIF-8 exhibits rougher skeleton surface compared with the parent 3DOM ZnO, suggesting the conversion from ZnO to ZIF-8. The amplified TEM observation in Fig. 2d clearly shows that the 3DOM ZIF-8 framework was constituted by massive nanosized ZIF-8 subunits in average size of ~ 20 nm. The STEM and corresponding elemental mapping images indicate the uniform elements distribution of Zn, C, and N, confirming the well-established 3DOM ZIF-8 framework (Fig. 2e–i). For comparison, ZIF-8 nanoparticles were also prepared through conventional wet-chemistry synthesis (see details in Experimental). Fig. S3 displays the typical dodecahedron morphology of ZIF-8 with an average particle size of ~ 200 nm. The size and morphology differences between 3DOM ZIF-8 and conventional ZIF-8 bulks are expected to be aroused by the spatial competition effect upon the coordination process. The ZnO skeleton provides a highly densified nucleation sites, which fiercely compete for the ligands with the adjacent sites, thus constraining the growth of each ZIF-8 particle with a resultant smaller crystal size. Whereas in conventional wet-chemistry synthesis, each Zn ion is highly exposed to the ligand with sparse Zn competitors around, leading to a much more dispersed nucleation and less constrained crystal growth. Apparently, compared with the bulk ZIF-8 particles, the 3DOM ZIF-8 architecture could expose more active

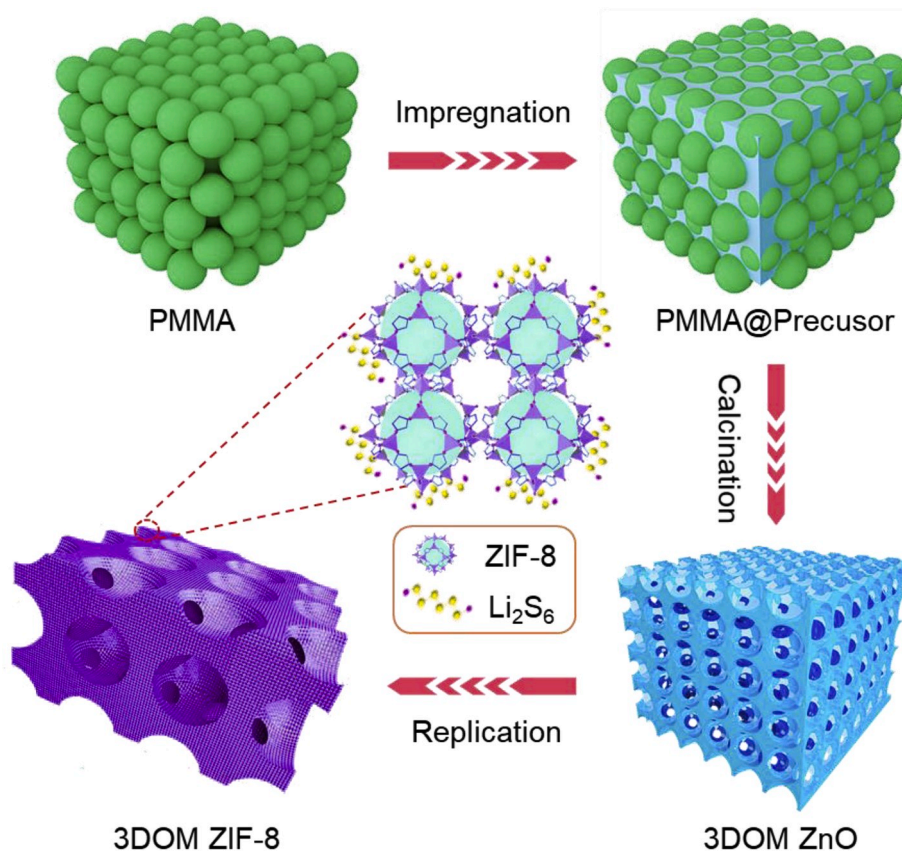


Fig. 1. Schematic illustration of 3DOM ZIF-8 synthesis process.

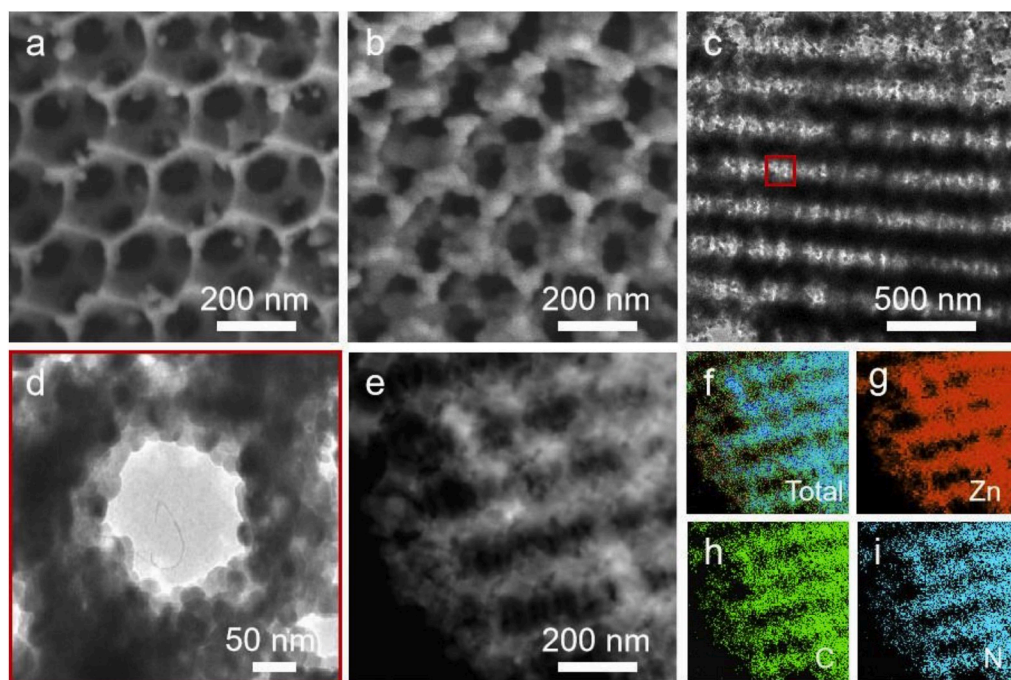


Fig. 2. SEM image of (a) 3DOM ZnO and (b) 3DOM ZIF-8; (c, d) TEM images of 3DOM ZIF-8; (e–i) STEM image of 3DOM ZIF-8 and corresponding elemental mappings of Zn, C and N.

interfaces due to the downsizing effect, as well as facilitated electrolyte infiltration and ion/mass transfer benefiting from the enhanced macroporosity.

Fig. 3a displays the XRD patterns of ZIF-8 and 3DOM ZIF-8. Characteristic diffraction peaks can be found between 5° – 20° for both ZIF-8 and 3DOM ZIF-8, demonstrating the successful formation of ZIF-8 crystal [14]. Meanwhile, the XRD pattern of 3DOM ZnO is also presented in Fig. S4, which can be well indexed to the crystalline ZnO in hexagonal structure (JCPDS No.75–0576). The absence of ZnO peaks in

3DOM ZIF-8 (Fig. 3a) confirms the complete phase conversion. The porous textures of the products were studied by N_2 adsorption-desorption measurement. The ZIF-8 exhibits a predominant microporosity with a high surface area of $1218 \text{ m}^2 \text{ g}^{-1}$ and concentrated pore size distribution within the range below 2 nm. By contrast, the 3DOM ZIF-8 shows a typical type-I isotherm curve, demonstrating higher pore size distributions at meso- and macroporous range with a resultant lower surface area of $962 \text{ m}^2 \text{ g}^{-1}$ and higher pore volume compared with ZIF-8 (0.63 vs. $0.35 \text{ m}^3 \text{ g}^{-1}$) (Fig. 3b and c). This result

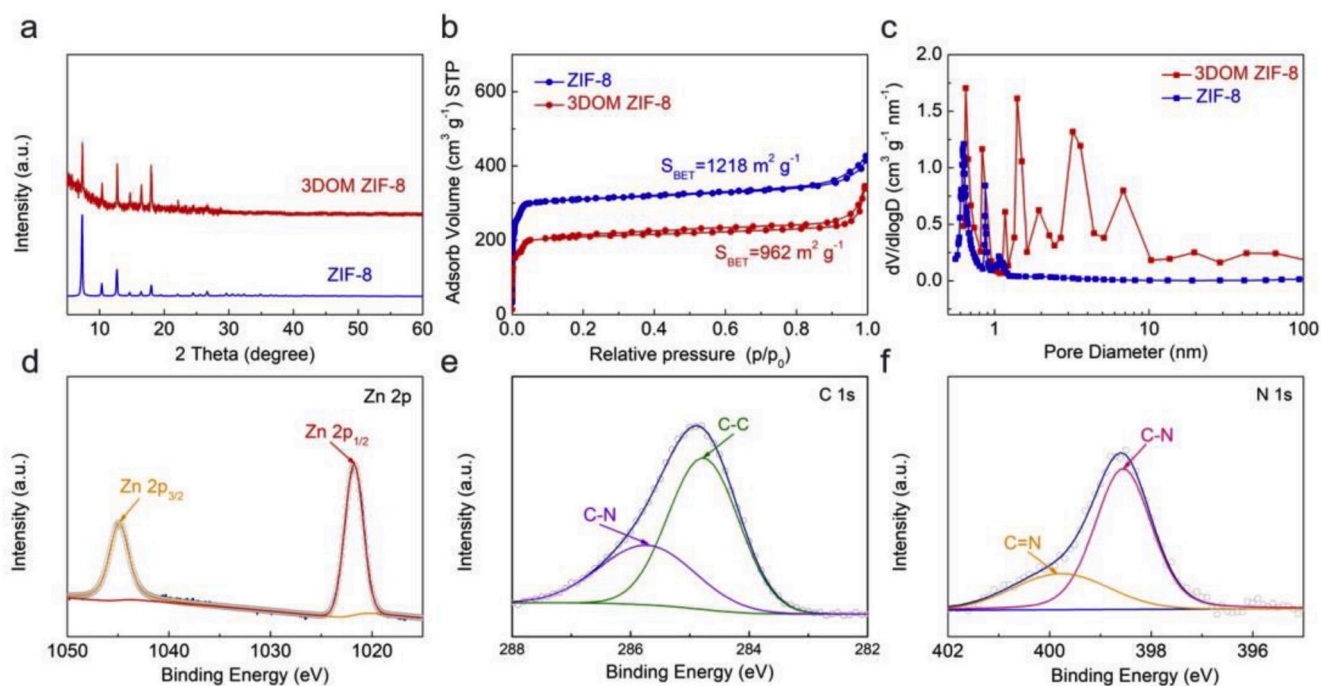


Fig. 3. (a) XRD patterns, (b) N_2 adsorption-desorption isotherms, and (c) pore size distribution of ZIF-8 and 3DOM ZIF-8; (d–f) Zn 2p, C 1s and N 1s high-resolution XPS spectra of 3DOM ZIF-8.

confirms the enhancement in meso/macroporosity through the construction of 3DOM architecture, which is expected to facilitate the sulfur accommodation, electrolyte infiltration, and ion/mass transfers. Meanwhile, the relatively high surface area compared with 3DOM ZnO (Fig. S5) could also provide abundant active sites for sulfur interfacial reactions.

Apart from that, the surface chemistry of the obtained 3DOM ZIF-8 was studied by XPS analysis. As shown in Fig. 3d, the Zn 2p XPS spectrum shows two peaks at 1021.7 and 1044.9 eV, corresponding to Zn 2p_{1/2} and Zn 2p_{3/2}, respectively [25]. The C 1s spectrum demonstrates two sub-peaks (Fig. 3e) assigned to the C–C (284.8 eV) and the C–N bond (285.7 eV) [26]. Meanwhile, the N 1s spectrum can be also deconvoluted into two peaks at 398.6 and 399.8 eV, which are attributed to the C–N and C=N bond, respectively (Fig. 3f) [27]. These results confirm the coordination between Zn²⁺ and organic ligands to form the ZIF-8 crystal in the product. Fig. S6 presents the FTIR spectra of 3DOM ZnO and 3DOM ZIF-8. Compared with ZnO, the spectrum of 3DOM ZIF witnesses the disappearance of Zn–O peak (467 cm⁻¹) accompanied by the emergence of Zn–N peak (415 cm⁻¹) [28]. Besides, new peak groups assigned to the C–H (2800–3200 cm⁻¹) and imidazole rings (600–1550 cm⁻¹) can be also observed in 3DOM ZIF-8 spectrum [29,30]. These results strongly confirm the successful conversion of ZnO into ZIF-8 framework structure through the coordination-replication method.

To evaluate the as-developed 3DOM ZIF-8 as sulfur host material in Li–S batteries, S/3DOM ZIF-8 composite was firstly prepared via conventional melt-impregnation method (see details in Experimental). A set of characteristic peaks of crystalline sulfur (JCPDS No.08–0247) can be

observed in both S/ZIF-8 and S/3DOM ZIF-8 composites, indicating the successful sulfur loading in the host materials (Fig. S7). The SEM and the corresponding elemental mapping images reveal the homogeneous sulfur distribution in S/3DOM ZIF-8 as shown in Fig. S8. The sulfur content was determined ca. 64.87 wt% and 66.54 wt% in S/ZIF-8 and S/3DOM ZIF-8 composites, respectively, by thermogravimetric analysis (TGA) as shown in Fig. S9.

Sulfur electrodes based on the obtained composite materials were prepared and assembled in CR2032 type coin cells for electrochemical evaluation. Fig. 4a displays the typical CV curves of S/3DOM ZIF-8 electrode at 0.1 mV s⁻¹. Two characteristic cathodic peaks and one anodic peak can be observed, corresponding to the typical sulfur redox reactions. Specifically, the two cathodic peaks at 2.31 and 2.06 V (vs. Li/Li⁺, hereinafter inclusive) refer to the reduction of S₈ into the soluble Li₂S_n (4 ≤ n ≤ 8) and the further reduction into the insoluble Li₂S₂/Li₂S, respectively. Meanwhile, the overlapped anodic peak at 2.33 V is ascribed to the oxidation of Li₂S₂/Li₂S to S₈. Compared with S/ZIF-8 electrode (Fig. S10), S/3DOM ZIF-8 electrode exhibits higher intensity and reproducibility of the CV peaks, indicating its superior cyclic stability. Consistently, the galvanostatic discharge-charge (GCD) profiles of S/3DOM ZIF-8 electrode display two discharge plateaus at 2.08 and 2.32 V and one charge plateau at around 2.33 V (Fig. 4b). Comparing with the S/ZIF-8 counterpart (Fig. 4c), the S/3DOM ZIF-8 electrode exhibits much higher discharge capacity (1220 vs. 1060 mAh g⁻¹), indicating a significantly enhanced sulfur utilization. Moreover, S/3DOM ZIF-8 demonstrates lower potential hysteresis (ΔV) than S/ZIF-8 (0.15 vs. 0.21 V), implying its faster electrochemical reaction kinetics.

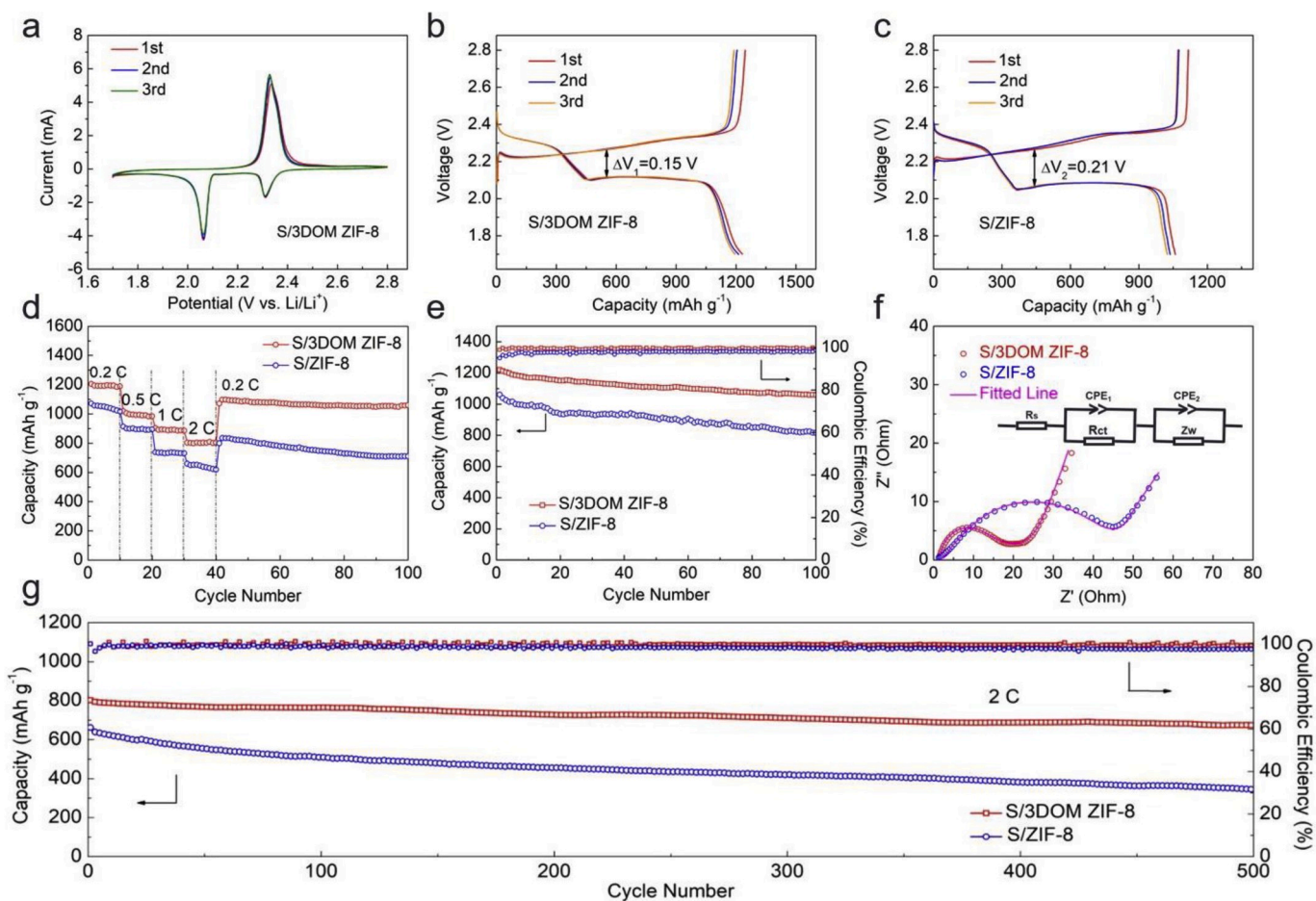


Fig. 4. (a) CV curves of S/3DOM ZIF-8 at 0.1 mV s⁻¹; galvanostatic charge/discharge profiles of (b) S/3DOM ZIF-8 and (c) S/ZIF-8 electrodes at 0.2 C; (d) rate performance, (e) cycling performance at 0.2 C, (f) Nyquist plots and the equivalent circuit model (inset) and (g) long-term cycling performance at 2 C of S/ZIF-8 and S/3DOM ZIF-8 electrodes.

Apart from that, the rate performances and the corresponding GCD profiles of different electrodes are presented in Fig. 4d and Fig. S11. The S/ZIF-8 electrode undergoes a rapid capacity decaying along with the increase of current rate, retaining a relatively low capacity of 659 mA h g⁻¹ at 2 C. By contrast, the S/3DOM ZIF-8 electrode is capable of maintaining a high capacity of 803 mA h g⁻¹ at 2 C, which can be recovered to 1070 mA h g⁻¹ as the current returns to 0.2 C, strongly indicating the superior sulfur reaction kinetics as well as the excellent electrochemical reversibility in the 3DOM ZIF-8 matrix. Such kinetic improvement can be further perceived from the GCD profile comparison as shown in Figs. S11 and S12. It is worth noting that the S/3DOM ZIF-8 electrode delivers much smaller electrochemical polarization with less voltage hysteresis upon the multi-rate cycling test compared with S/ZIF-8 electrode, verifying the catalyzed sulfur redox reactions in 3DOM ZIF-8.

Fig. 4e and Fig. S13 present the cycling performances of S/3DOM ZIF-8 and S/ZIF-8 electrodes at 0.2 and 1 C. In comparison, the S/3DOM ZIF-8 electrode exhibits a significantly improved cycling stability with a higher capacity retention of 1060 mA h g⁻¹ than the S/ZIF-8 electrode (815 mA h g⁻¹) after 100 cycles. The well-defined 3D ordered porous architecture can be maintained after cycling, indicating the good structural integrity of 3DOM ZIF-8 upon the battery operation (Fig. S14). The EIS spectra of different electrodes are depicted in Fig. 4f. The Nyquist plot consists of a depressed semicircle in the high-frequency region and a sloped line in the low-frequency region. The semicircle is associated with the charge transfer resistance (R_{ct}), while the linear slope refers to the Warburg impedance reflecting the Li⁺ diffusion rate [31,32]. Meanwhile, the electrolyte resistance (R_e) can be determined by the intercept on the Z' axis. The EIS results clearly reveal the smaller internal impedance of S/3DOM ZIF-8 electrode compared with that of S/ZIF-8, demonstrating the enhanced charge transfer kinetics. Furthermore, the long-term cyclic stability of different sulfur electrodes was also evaluated as shown in Fig. 4g. The S/3DOM ZIF-8 electrode delivers a high capacity of 674 mA h g⁻¹ after 500 cycles at 2 C, corresponding to a favorable capacity retention of 84% and an ultra-low fading rate of 0.028% per cycle. By contrast, the S/ZIF-8 counterpart suffers from serious capacity fading to 345 mA h g⁻¹ after 500 cycles with a poor capacity retention of 52.3%. Beyond that, a high coulombic efficiency close to a unity can be sustained upon the cycling for the S/3DOM ZIF-8 electrode, manifesting the effective inhibition on polysulfide shuttling and the commendable electrochemical reversibility. It should be noted that these electrochemical performances are highly competitive among the reported MOF-based sulfur electrode designs as shown in Table S1.

In order to understand the electrochemical improvement by 3DOM ZIF-8, the potential chemical interactions between 3DOM ZIF-8 and LiPS were studied by static LiPS adsorption test as shown in Fig. 5a. It can be observed that the pristine Li₂S₆ solution (0.1 M) shows a brown color, which turns into yellow and colorless after 12 h adsorption by ZIF-8 and 3DOM ZIF-8, respectively. Moreover, the UV-vis measurements on the supernatants before and after adsorption were also performed as shown in Fig. 5b. The characteristic peaks at 272 and 418 nm refer to the S₆²⁻ and S₄²⁻ species, respectively. By comparison, the solution adsorbed by 3DOM ZIF-8 exhibits more significantly weakened peaks, signifying its stronger adsorbability toward LiPS. The underlying chemical interactions between LiPS and 3DOM ZIF-8 were probed by XPS analysis (Fig. 5c). The S 2p spectrum of pure Li₂S₆ shows pairs of peaks at 161.7 and 163.4 eV, referring to the terminal (S_T⁻¹) and bridging sulfur (S_B⁰), respectively [33,34]. After adsorption by 3DOM ZIF-8, these peaks undergo considerable shift toward high binding energy (BE) region, suggesting the decreased electron cloud density of S [35]. Moreover, the Li 1s witnesses a new peak emerging at 56.0 eV in the spectrum of Li₂S₆ soaked 3DOM ZIF-8, which can be ascribed to the Li-N bonding, suggesting the formation of “lithium bond”-like interaction (Fig. 5d) [36]. The Zn 2p spectra also illustrate the shift of Zn 2p_{1/2} and Zn 2p_{3/2} peaks to lower BE region for Li₂S₆ soaked 3DOM ZIF-8 (Fig. S15), further manifesting the increased electron density at the metal center attributed to the Lewis acid-based interaction with LiPS [37]. All the above results confirm the strong chemical interactions between 3DOM ZIF-8 and LPS, which chemically confine the sulfur species against their dissolution and migration behaviors, thus contributing inhibited shuttle effect and prolonged cycling life for the according Li-S batteries.

To study kinetic improvement, the Li⁺ diffusion coefficients (D_{Li}^+) in different cells were characterized by CV measurements under varied scanning rates (Fig. 6a and b) based on the Randles Sevcik equation [38]:

$$D^{0.5} = \frac{1}{2690000 \times n^{1.5} \times A \times C} \times \frac{I_p}{\nu^{0.5}}$$

where I_p is the peak current; n refers to the number of electrons; A represents the electrode area; D refers to Li⁺ diffusion coefficient; C is the Li⁺ concentration; ν represents the scanning rate. The fitted straight slopes of peak current vs. $\nu^{0.5}$ were plotted to determine D_{Li}^+ as shown in Fig. 6c and d. Clearly, the S/3DOM ZIF-8 electrode delivers higher slopes for all the A, B, and C peaks in the CV profiles, corresponding to the much higher D_{Li}^+ than those of S/ZIF-8 (Fig. S16). This result strongly illustrates the significantly facilitated Li⁺ transfer behaviors in 3DOM

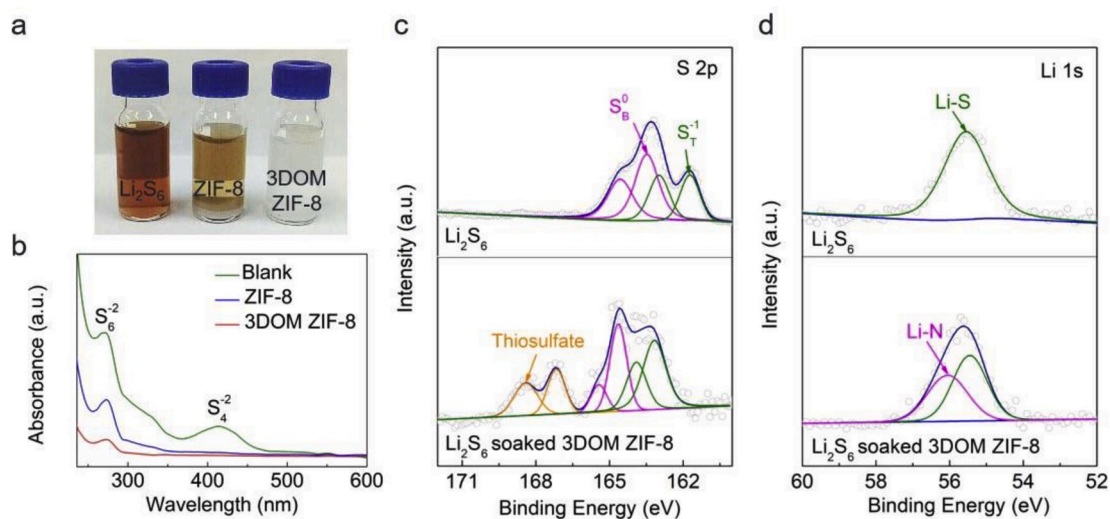


Fig. 5. (a) Optical observation and (b) UV-vis spectra of Li₂S₆ solution adsorbed by ZIF-8 and 3DOM ZIF-8; (c) S 2p and (d) Li 1s high-resolution XPS spectra of pristine Li₂S₆ and Li₂S₆ adsorbed by 3DOM ZIF-8.

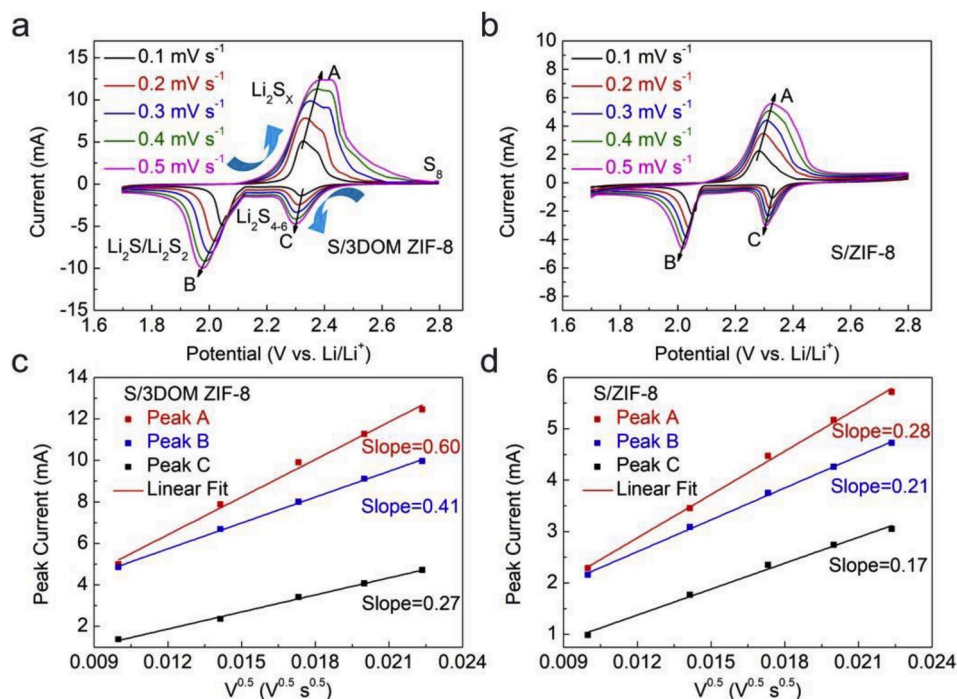


Fig. 6. CV curves at various voltage scan rates for (a) S/3DOM ZIF-8 and (b) S/ZIF-8 electrodes; fitting plots of peak current (I_p) versus the square root of the scan rate ($\nu^{0.5}$) for (c) S/3DOM ZIF-8 and (d) S/ZIF-8 electrodes.

ZIF-8 matrix attributed to its highly open macroporous architecture for facile electrolyte filtration, which expedites the Li^+ supply for sulfur reactions and propel a fast conversion kinetic. Further validation on the catalyzed sulfur reactions was performed using symmetric cells containing Li_2S_6 electrolytes and two identical electrodes. As shown in Fig. 7a, the symmetrical cell without Li_2S_6 shows negligible current response, verifying that the current originates from the LIPS redox reactions. Compared with ZIF-8 cell, the 3DOM ZIF-8 symmetric cell exhibits the highest current response with two clear redox peaks at $-0.48/0.48$ V and $-0.82/0.82$ V, confirming the significantly boosted LIPS conversions through the electrocatalytic effect. Such favorable effect by

3DOM ZIF-8 also exhibits good durability as demonstrated by the well overlapped CV curves upon the several cycles (Fig. 7b). The Nyquist plot of symmetric cells further verifies the improved redox kinetics, showing an obviously smaller charge transfer resistance for 3DOM ZIF-8 cell compared with that based on ZIF-8 (Fig. 7c).

In general, the Li_2S electrochemical redox has been considered as the most kinetic-constraining process in Li-S chemistry. Thus, the Li_2S oxidation and deposition behaviors were particularly evaluated for the kinetic study. LSV measurement was conducted in three-electrode configuration with 0.1 M Li_2S /methanol as electrolyte and Ag/AgCl as reference to specifically investigate the Li_2S oxidation behavior. As

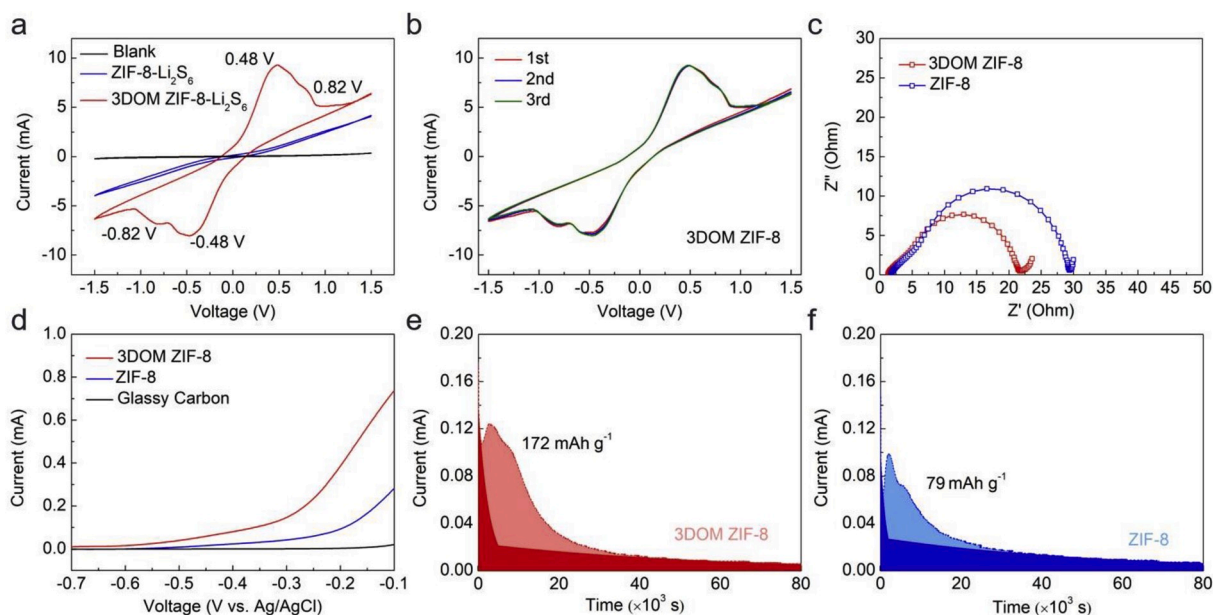


Fig. 7. (a) CV curves at scanning rate of 10 mV s^{-1} , (b) CV curves of 3DOM ZIF-8 at different cycles, and (c) EIS spectra of ZIF-8 and 3DOM ZIF-8 Li_2S_6 symmetric cells; (d) LSV curves of Li_2S oxidation for ZIF-8 and 3DOM ZIF-8 electrodes; Li_2S deposition profiles of (e) 3DOM ZIF-8 and (f) ZIF-8.

shown in Fig. 7d, the 3DOM ZIF-8 exhibits the smallest onset potential with the highest current response compared with ZIF-8 and glassy carbon, suggesting its lowest activation energy to electrochemically convert solid Li_2S to soluble LiPS on 3DOM ZIF-8 surface. In addition, the LiPS conversion into Li_2S was also probed on ZIF-8 and 3DOM ZIF-8 surface (Fig. 7e and f). Clearly, 3DOM ZIF-8 electrode exhibits much higher Li_2S precipitation capacity (172 mAh g^{-1}) than that of ZIF-8 (79 mAh g^{-1}), manifesting the considerably facilitated Li_2S nucleation and precipitation behaviors. These results cooperatively confirm the enhanced LiPS conversion kinetics on 3DOM ZIF-8 surface. Based on the above results, the strong chemical interactions between LiPS and 3DOM ZIF-8 impose effective sulfur confinement against the polysulfide shuttling as well as effective catalyzation on the sulfur conversion reactions, thus contributing to the significant improvement in cyclability and rate capability for the according Li-S batteries.

Given this, S/3DOM ZIF-8 electrode under high sulfur loading and limited electrolyte was further explored to pursue higher energy density for practical applications. S/3DOM ZIF-8 electrodes at sulfur loading of 2.0, 3.6, and 7.4 mg cm^{-2} were prepared with the thickness of around 34, 60 and $112 \text{ }\mu\text{m}$ (Fig. S17), and porosity of ca. 49.5%, 48.2%, and 41.8%, respectively [39]. Fig. 8a shows the GCD profiles of S/3DOM ZIF-8 electrode at 1st, 50th, 100th and 200th cycles with a high sulfur loading of 7.4 mg cm^{-2} and small E/S ratio of 4.25 mL g^{-1} . The electrode well maintains the typical voltage profile of sulfur redox with the second discharge plateau at 2.01 V, demonstrating the limited potential hysteresis and rapid sulfur reaction kinetics. Moreover, the rate performance of S/3DOM ZIF-8 electrodes under sulfur loading of 3.6 and 7.4 mg cm^{-2} and respective E/S ratio of 8.74 and 4.25 mL g^{-1} were also evaluated by multi-rate cycling as shown in Fig. 8b. The results show that the as-developed sulfur electrodes are capable of withstanding a high rate up to 2 C under these conditions (Fig. 8b) attributed the favorable mass/charge transfer and the catalyzed sulfur redox reactions in 3DOM ZIF-8 matrix. Fig. 8c depicts the cycling behavior of S/3DOM ZIF-8 electrode, which delivers initial high areal capacities of 3.6 and 5.8 mAh cm^{-2} , with a capacity retention of 2.8 and 4.5 mAh cm^{-2} respectively, after 200 cycles. The SEM images reveal the well-maintained macroporous architecture for the high-loading S/3DOM ZIF-8 electrode (7.4 mg cm^{-2}) after cycling, indicating the

good structural integrity (Fig. S18). Meanwhile, a basically uniform SEI layer can be obtained on Li surface without obvious dendrite growth, demonstrating the suppressed electrolyte depletion and lithium corrosion. However, relatively rougher and more porous Li surface can be still observed after cycling, which calls for further advances in anode protection and stabilization. The decent rate and cycling performance under high sulfur loading and limited electrolyte can be ascribed to the synergistic combination of the architectural and chemical advantages of 3DOM ZIF-8, which propels efficient sulfur utilization, rapid redox reactions, and strong sulfur confinement towards a fast and durable sulfur electrochemistry. For a demonstration, the Li-S battery based on the S/3DOM ZIF-8 electrode was applied to power six light-emitting diodes over 30 min without brightness loss (Fig. 8d), manifesting the good promise of the as-developed material design in promoting the high-performance and practically viable Li-S batteries.

4. Conclusions

In summary, we have developed an advanced 3DOM ZIF-8 material as multifunctional sulfur host towards high-efficiency Li-S batteries. The synergistic combination of macroporous 3DOM framework and microporous ZIF-8 nanoparticles not only facilitates the electrolyte infiltration for expedite mass/charge transportation, but also homogenizes sulfur distribution and suppresses sulfur dissolution for enhanced sulfur utilization. In addition, the abundant active interfaces in 3DOM ZIF-8 offer strong LiPS adsorption via the Lewis acid-base interactions as well as beneficial catalytic effect for LiPS conversion, leading to significant inhibition on polysulfides shuttling as well as favorable promotion on sulfur redox reaction kinetics. As a result, the S/3DOM ZIF-8 electrodes deliver outstanding cyclic stability with a low capacity decay of 0.028% per cycle over 500 cycles, as well as decent areal capacity ($>6 \text{ mAh cm}^{-2}$) and cyclability under high loading (7.4 mg cm^{-2}) and limited electrolyte ($\text{E/S} = 4.25 \text{ mL g}^{-1}$). The successful implantation of 3DOM ZIF-8 in Li-S batteries offers a new route to designing advanced electrode materials for high-performance Li-S batteries, which could be also extended to other related fields such as electro-catalysis, supercapacitor, and metal-air batteries.

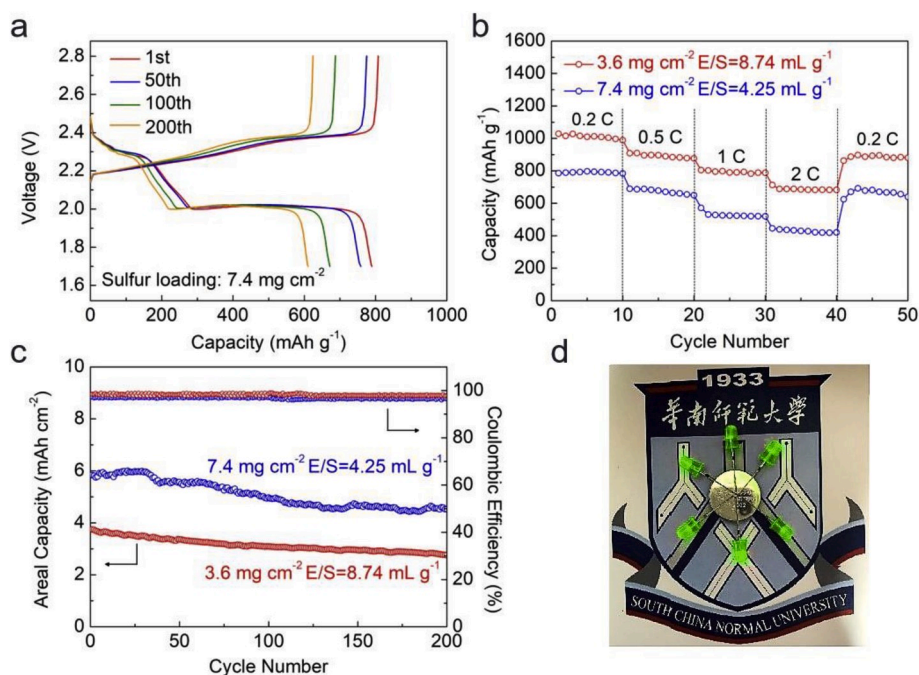


Fig. 8. (a) GCD profiles at 0.2 C, (b) rate performance, and (c) cycling performance at 0.2 C of S/3DOM ZIF-8 electrodes under high sulfur loading and limited electrolyte; (d) photograph of light-emitting diodes (LEDs) powered by Li-S battery based on S/3DOM ZIF-8 cathode.

Declaration of competing interest

The authors declare that they have no known competing financial interests or personal relationships that could have appeared to influence the work reported in this paper.

CRediT authorship contribution statement

Guoliang Cui: Conceptualization, Methodology, Data curation, Writing - original draft, Visualization, Investigation, Validation, Writing - review & editing. **Gaoran Li:** Conceptualization, Methodology, Data curation, Writing - original draft, Validation, Writing - review & editing. **Dan Luo:** Data curation, Writing - original draft, Visualization, Investigation. **Yongguang Zhang:** Conceptualization, Methodology, Visualization, Investigation, Supervision, Validation, Writing - review & editing. **Yan Zhao:** Data curation, Writing - original draft, Visualization, Investigation. **Daorui Wang:** Data curation, Writing - original draft. **Jiayi Wang:** Data curation, Writing - original draft. **Zhen Zhang:** Data curation, Writing - original draft. **Xin Wang:** Visualization, Investigation, Supervision, Validation, Writing - review & editing. **Zhongwei Chen:** Conceptualization, Methodology, Supervision, Validation, Writing - review & editing.

Acknowledgments

This work was supported by the National Natural Science Foundation of China Program (No. 51602111 and Nos. U1909213); Program for the Outstanding Young Talents of Hebei Province, China (YG.Z.); Chunhui Project of Ministry of Education of the People's Republic of China (Grant No. Z2017010); Xijiang R&D Team (X.W.), Guangdong Innovative and Entrepreneurial Team Program (No. 2016ZT06C517), and Science and Technology Program of Guangzhou (No. 2019050001). The authors also thank the support from Natural Sciences and Engineering Research Council of Canada, University of Waterloo, and Waterloo Institute for Nanotechnology, University of Waterloo.

Appendix A. Supplementary data

Supplementary data to this article can be found online at <https://doi.org/10.1016/j.nanoen.2020.104685>.

References

- [1] S. Wang, J. Liao, X. Yang, J. Liang, Q. Sun, J. Liang, F. Zhao, A. Koo, F. Kong, Y. Yao, X. Gao, M. Wu, S.-Z. Yang, R. Li, X. Sun, *Nano Energy* 57 (2019) 230–240.
- [2] D. Luo, G. Li, Y.-P. Deng, Y. Zhang, J. Li, R. Liang, M. Li, Y. Jiang, W. Zhang, Y. Liu, W. Lei, A. Yu, Z. Chen, *Adv. Energy Mater.* 9 (2019) 1900228.
- [3] G. Li, W. Lei, D. Luo, Y.-P. Deng, D. Wang, Z. Chen, *Adv. Energy Mater.* 8 (2018) 1702381.
- [4] Y. Tian, Y. Zhao, Y. Zhang, L. Ricardez-Sandoval, X. Wang, J. Li, *ACS Appl. Mater. Interfaces* 11 (2019) 23271.
- [5] A. Rosenman, E. Markevich, G. Salitra, D. Aurbach, A. Garsuch, F.F. Chesneau, *Adv. Energy Mater.* 5 (2015) 1500212.
- [6] M. Wild, L. O'Neill, T. Zhang, R. Purkayastha, G. Minton, M. Marinescu, G.J. Offer, *Energy Environ. Sci.* 8 (2015) 3477–3494.
- [7] G. Li, W. Lei, D. Luo, Y. Deng, Z. Deng, D. Wang, A. Yu, Z. Chen, *Energy Environ. Sci.* 11 (2018) 2372–2381.
- [8] Z. Cheng, H. Pan, H. Zhong, Z. Xiao, X. Li, R. Wang, *Adv. Funct. Mater.* 28 (2018) 1707597.
- [9] K. Park, J.H. Cho, J.-H. Jang, B.-C. Yu, A.T. Hoz, K.M. Miller, C.J. Ellison, J. B. Goodenough, *Energy Environ. Sci.* 8 (2015) 2389–2395.
- [10] J. Zhang, G. Jiang, T. Cumberland, P. Xu, Y. Wu, S. Delaat, A. Yu, Z. Chen, *InfoMat* 1 (2019) 234–241.
- [11] Z. Li, C. Li, X. Ge, J. Ma, Z. Zhang, Q. Li, C. Wang, L. Yin, *Nano Energy* 23 (2016) 15–26.
- [12] Z. Wang, X. Li, Y. Cui, Y. Yang, H. Pan, Z. Wang, C. Wu, B. Chen, G. Qian, *Cryst. Growth Des.* 13 (2013) 5116–5120.
- [13] J. Wang, L. Si, Q. Wei, X. Hong, L. Lin, X. Li, J. Chen, P. Wen, Y. Cai, *J. Energy Chem.* 28 (2019) 54–60.
- [14] B.-Q. Li, H.-J. Peng, X. Chen, S.-Y. Zhang, J. Xie, C.-X. Zhao, Q. Zhang, *CCS Chem* 1 (2019) 128–137.
- [15] X. Hu, J. Jian, Z. Fang, L. Zhong, Z. Yuan, M. Yang, S. Ren, Q. Zhang, X. Chen, D. Yu, *Energy Storage Mater.* 22 (2019) 40–47.
- [16] S. Bai, X. Liu, K. Zhu, S. Wu, H. Zhou, *Nat. Energy* 1 (2016) 16094.
- [17] J. Zhou, R. Li, X. Fan, Y. Chen, R. Han, W. Li, J. Zheng, B. Wang, X. Li, *Energy Environ. Sci.* 7 (2014) 2715–2724.
- [18] H. Park, D.J. Siegel, *Chem. Mater.* 29 (2017) 4932–4939.
- [19] Z. Wang, B. Wang, Y. Yang, Y. Cui, Z. Wang, B. Chen, G. Qian, *ACS Appl. Mater. Interfaces* 7 (2015) 20999–21004.
- [20] X. Zhou, L. Chen, W. Zhang, J. Wang, Z. Liu, S. Zeng, R. Xu, Y. Wu, S. Ye, Y. Feng, X. Cheng, Z. Peng, X. Li, Y. Yu, *Nano Lett.* 19 (2019) 4965–4973.
- [21] X. Zhao, P. Pachfule, S. Li, T. Langenhahn, M. Ye, C. Schlesiger, S. Praetz, J. Schmidt, A. Thomas, *J. Am. Chem. Soc.* 141 (2019) 6623–6630.
- [22] K. Shen, L. Zhang, X. Chen, L. Liu, D. Zhang, Y. Han, J. Chen, J. Long, R. Luque, Y. Li, B. Chen, *Science* 359 (2018) 206–210.
- [23] J. Xie, H.J. Peng, J.Q. Huang, W.T. Xu, X. Chen, Q. Zhang, *Angew. Chem. Int. Ed. Engl.* 56 (2017) 16223–16227.
- [24] G. Liu, J. Li, J. Fu, G. Jiang, G. Lui, D. Luo, Y.-P. Deng, J. Zhang, Z.-P. Cano, A. Yu, D. Su, Z. Bai, L. Yang, Z. Chen, *Adv. Mater.* 31 (2019) 1806761.
- [25] P. Tian, K. Shen, J. Chen, T. Fan, R. Fang, Y. Li, *Small Methods* 2 (2018) 1800219.
- [26] W. Cai, G. Li, D. Luo, G. Xiao, S. Zhu, Y. Zhao, Z. Chen, Y. Zhu, Y. Qian, *Adv. Energy Mater.* 8 (2018) 1802561.
- [27] J. Zhang, G. Li, Y. Zhang, W. Zhang, X. Wang, Y. Zhao, J. Li, Z. Chen, *Nano Energy* 64 (2019) 103905.
- [28] S. Mukhopadhyay, J. Debgupta, C. Singh, A. Kar, S.-K. Das, *Angew. Chem.* 130 (2018) 1936–1941.
- [29] S. Liu, F. Chen, S. Li, X. Peng, Y. Xiong, *Appl. Catal., B* 211 (2017) 1–10.
- [30] J. Wang, G. Han, L. Wang, L. Du, G. Chen, Y. Gao, Y. Ma, C. Du, X. Cheng, P. Zuo, *Small* 14 (2018) 1704282.
- [31] Z. Wang, B. Wang, Y. Yang, Y. Cui, Z. Wang, B. Chen, G. Qian, *ACS Appl. Mater. Interfaces* 7 (2015) 20999–21004.
- [32] D. Luo, Y.P. Deng, X. Wang, G. Li, J. Wu, J. Fu, W. Lei, R. Liang, Y. Liu, Y. Ding, A. Yu, Z. Chen, *ACS Nano* 11 (2017) 11521–11530.
- [33] Y.-L. Ding, P. Kopold, K. Hahn, P.A. van Aken, J. Maier, Y. Yu, *Adv. Funct. Mater.* 26 (2016) 1112–1119.
- [34] R.V. Bugga, S.C. Jones, J. Pasalic, C.S. Seu, J.-P. Jones, L. Torres, *J. Electrochem. Soc.* 164 (2016) 265–276.
- [35] J. Wang, J. Liang, J. Wu, C. Xuan, Z. Wu, X. Guo, C. Lai, Y. Zhu, D. Wang, *J. Mater. Chem.* 6 (2018) 6503–6509.
- [36] Y. Wang, R. Zhang, J. Chen, H. Wu, S. Lu, K. Wang, H. Li, C. Harris, K. Xi, R. Kumar, S. Ding, *Adv. Energy Mater.* 9 (2019) 1900953.
- [37] H. Liu, Z. Chen, L. Zhou, K. Pei, P. Xu, L. Xin, Q. Zeng, J. Zhang, R. Wu, F. Fang, R. Che, D. Sun, *Adv. Energy Mater.* 9 (2019) 1901167.
- [38] Y. Wang, R. Luo, Y. Zhang, Y. Guo, Y. Lu, X. Liu, J.-K. Kim, Y. Luo, *ACS Appl. Energy Mater.* 2 (2019) 3314–3322.
- [39] N. Kang, Y. Lin, L. Yang, D. Lu, J. Xiao, Y. Qi, M. Cai, *Nat. Commun.* 10 (2019) 4597.